BIBECHANA
Vol. 21, No. 1, April 2024, 37–50

ISSN 2091-0762 (Print), 2382-5340 (Online)
Journal homepage: http://nepjol.info/index.php/BIBECHANA
Publisher:Dept. of Phys., Mahendra Morang A. M. Campus (Tribhuvan University)Biratnagar

Comparative study of the dust color temperature and dust mass within the isolated dust in W51 giant molecular cloud in IRIS and AKARI data

M. S. Paudel[1,*], H. K. Kushuwala[1], S. Bhattarai[2]

[1]*Department of Physics, Tri-Chandra Multiple Campus, Tribhuvan University, Nepal*
[2]*Central Department of Physics, Tribhuvan University, Nepal*

[*]Corresponding author. Email: mspaudel27@gmail.com,madhu.paudel@trc.tu.edu.np

Abstract

This work presents the comparative study of the properties of dust within the W51 Giant Molecular Cloud (GMC) located at (RA, DEC) (J2000): 290.91°, +14.51°. *In the infrared data of Improved Reprocessing of the IRAS (IRIS) the dust structure seems single and isolated having size* $0.45° \times 0.45°$ *but in AKARI infrared survey it breaks into two isolated regions having size* $0.15° \times 0.15°$ *and* $0.10° \times 0.10°$*, represented by AKARI-I and AKARI-II respectively. In IRIS map,* 60 *and* 100 μm *and in AKARI map,* 90 *and* 140 μm *image are used for extraction of the infrared flux. The dust color temperature* (T_d) *and dust mass* (M_d) *are calculated from the infrared flux and found to be* 30.34 *K in IRIS and* 27.40 *K and* 23.55 *K in AKARI-I and AKARI-II. A linear relationship between the infrared flux at two wavelengths is found except AKARI-I. The dust mass per pixel in the isolated (core) region is found to be increased compared to the total study region. To quantify the relation between flux, dust color temperature, and dust mass, the regression analysis is used and observed spectrum of relation. A huge SIMBAD background objected is found embedded in the dust cloud which might have been shaping the spatial variation of temperature and mass within the dust cloud.*

Keywords
W51 Giant Molecular Cloud, Infrared flux, Dust Color Temperature, Dust Mass, IRIS, AKARI.

Article information
Manuscript received: September 26, 2023; Revised: December 17, 2023; Accepted: December 25, 2023
DOI https://doi.org/10.3126/bibechana.v21i1.58815

1 Introduction

A Giant Molecular Cloud (GMC) is a huge structure in the interstellar medium that can nurture the various phases of star formation, often called the stellar nursery. It is believed that the massive stars are formed in GMC in the Milky Way Galaxy [1]. However, the formation of the star from the natal GMC is still an unclear topic. W51 is an example of the GMC in the Milky Way Galaxy located at the Sagittarius arm of the Galaxy [2]. It is found from the latest research that an active and massive star is forming in the W51 molecular cloud. In the Milky Way Galaxy, W51 is in the top 1% by size, top (5-10)% by mass [3], and top (50-15)% by star formation efficiency (SFE) [4]. It is found that the majority of the star has been formed within $\sim$ 3 Myr. Many HII and Cluster are embedded within the cloud. Moreover, W51 is hosting many objects which are revealed at different wavelengths, such as; various newly formed O stars are detected in the near-infrared wavelength, many third-generation of the massive proto-stars are detected in the mid-infrared wavelength, and numerous young stellar populations are detected in the microwave, millimeter, and submillimeter wavelengths [5].

The infrared astronomy is crucial to explore the part of the Galaxy into those parts where the visible light is unable to reach. In the history of infrared astronomy, Infrared Astronomical Satellite (IRAS) was the first space satellite which was successful in mapping more than 96% of the Milky Way Galaxy in the infrared (IR) wavelength [6]. Infrared radiation is emitted by the hot dust molecules in Inter-Stellar Medium (ISM) due to the absorption of energetic radiation, such as; X-ray, Ultra-Violet (UV), and visible ray emitted from nearby hot star and stellar remnants. The mass budget of the interstellar dust can be studied via infrared radiation. It is believed that the dominant dust formation mechanisms are the stellar wind created mass loss in AGB phase and Supernova Remnants (SNRs) phase of stellar evolution and in ISM, its abundance increases by coagulation, erosion, shattering, etc. [7, 8].

There have been many studies concerning the properties of dust using the infrared data from IRAS, Improved Reprocessing of IRAS Survey (IRIS) [9], AKARI [10], and Wide Infrared Survey Explorer (WISE) [11]. Recently, the properties of the North-East part of the Perseus molecular cloud is studied by Bhattarai et al., (2023) [12] using IRIS and AKARI data, in which the dust color temperature (T_d) in IRIS data (26.34 ± 0.11 K) is found higher than the AKARI data (17.63 ± 0.02 K) but the dust mass (M_d) is found higher in AKARI data. The spatial distribution of the infrared flux and temperature is almost similar in both IRIS and AKARI data but for dust mass and visual extinction there is a huge difference between both data. Also, many background sources, such as; dense core, part of cloud, submillimeter Radio source, IR, dark and reflection nebula, etc., are found within the studied region which are considered as the major contributor of the dust mass.

In most of the studies T_d is found between 15 K and 45 K in IRAS/IRIS data, such as; 20 K to 24 K for the dust cloud nearby WD 0307+077 [13], 22.91 K to 34.58 K for the dust nearby PG 1225-079 [14], 25.59 K to 36.82 K for the dust nearby WD 0011-399 [15], 22.67 K to 33.56 K for the dust nearby the Supernova Remnants (SNRs) in Galactic plane [16], 21.87 K to 24.09 K for the dust nearby WD 0352-049 [17], 23.77 K to 24.93 K nearby C-rich AGB star 19558+3333 [18], 20.75 to 35.90 K and 22.52 to 45.63 for the dust in two different nebula [19]. In AKARI data T_d is also found in the same range, such as; 17.87 K to 43.47 K nearby PG 1225-079 [14], 16.31 K to 26.37 nearby WD 0011-399 [15] and 15.78 K to 28.86 nearby SNRs in Galactic planes [16] and 16.78 K to 17.71 nearby C-rich AGB star 19558+3333 [18]. However, the average value of T_d is found less in AKARI data compared to IRAS/IRIS in all data. For WISE data, T_d is found between 286.38 K nearby PG 1225-079 [14], 307.24 K to 353.72 K nearby WD 0011-399 [15], 122.55 K to 125.11 K nearby C-rich AGB star 19558+3333 [18]. A higher value of T_d is observed in WISE data. In most of the work, the relationship between the temperature and mass of dust is trying to explain. In dust clouds around WD 0352-044 in IRIS data [17], dust cloud around SNRs in AKARI data [16], dust clouds around PG 1225-079 in WISE and AKARI data [14], dust cloud around WD 0011-399 in WISE data [15] the temperature and mass have an inverse relation, means higher dust mass is observed in the color map where the temperature is low and vice-versa. There are some other works in which no preferred relationship between T_d and M_d is found, for instance, dust cloud around SNRs in IRIS data [16], dust cloud around WD 0011-399 in IRIS and AKARI data [15], dust cloud around PG 1227-079 in IRIS data [14], etc. The inter-relationship between T_d and M_d is found independent of the infrared survey, such as; IRIS, AKARI, and WISE. More study is required for a clear conclusion.

This work focused on the investigation of T_d and M_d from infrared flux within the W51 molecular cloud. Infrared flux is used to calculate T_d and M_d and their distribution is analyzed. The relationship of the infrared flux with T_d and M_d as well as the between T_d and M_d is presented. The impact of the background objects embedded within the dust cloud is tried to explain.

2 Sources of Data

The major data used for this work is Flexible Image Transport System (FITS) images of infrared flux downloaded from SkyView Virtual Observatory (https://skyview.gsfc.nasa.gov/), for both IRIS [9] and AKARI [10]. Fig.1 shows the JPEG image at a longer wavelength, i.e., 100 μm in IRIS and 140 μm in AKARI. The distance of the W51 molecular cloud is taken from Genzel et al. (1981) [20]. The data from Set of Identification, Measurement Bibliography for Astronomical Data (SIMBAD) [https://simbad.u-strasbg.fr/simbad/sim-fid] [21] is used to study the background objects around the study region.

3 Method of Analysis

3.1 Infrared Flux and Dust Color Temperature

The Planck's law of blackbody spectrum gives the expression for the energy density emitted from a source in a wide range of the wavelength. The Planck's law can be modified to apply for interstellar dust assuming (i) the beam emitted from each pixel in the infrared map is isothermal in nature and (ii) the beam is in thermal equilibrium along the line of sight. With these assumptions, the flux density F_{λ_i} at wavelength λ_i is given as; [22, 23]

$$F_{\lambda_i} = \left[\frac{2hc}{\lambda_i^3}\left(\frac{1}{e^{\left(\frac{hc}{\lambda_i k_B T_d}\right)}-1}\right)\right] N_d \alpha \lambda_i^{-\beta} \Omega_i, \quad (1)$$

where T_d is the dust color temperature, N_d is the column density of the dust grains, α is a constant related to the optical depth of the dust, β is the spectral emissivity index, and Ω_i is the solid angle subtended at λ_i by the detector.

Using equation (1), the ratio of the infrared flux at two wavelengths, $F_{\lambda_1}/F_{\lambda_2}$, can be modified under the assumptions that $\Omega_{\lambda_1} \approx \Omega_{\lambda_2}$ and for low dust color temperature, T_d, we obtain,

$$T_d = \frac{-p}{\ln\left[R \times q^{(3+\beta)}\right]} \quad (2)$$

where, $p = 96$ for IRIS and 57 for AKARI data, $q = 0.6$ for IRIS and 0.64 for AKARI data, β is the spectral emissivity index. Also, the value of the wavelengths, λ_1 and λ_2, taken in this work are 60 μm and 100 μm for IRIS and 90 μm and 140 μm for AKARI data.

3.2 Dust Mass

The mass of dust in the molecular cloud can be obtained from the dust color temperature size of dust grain. The Planck's function at long wavelength can be used to estimate the dust mass more accurately. The expression of dust mass including all these quantities is given as [24, 25];

$$M_{\rm dust} = 0.4\left[\frac{S_\nu D^2}{B(\nu, T_d)}\right], \quad (3)$$

where S_ν is the absolute value of flux at long wavelength, D is the distance to the dust cloud, $B(\nu, T_d)$ is the Planck's function for the blackbody radiation.

Once the mass of dust is estimated from equation (3), the dust-to-gas ratio, $M_{\rm gas} \approx 150 M_{\rm dust}$ [24], is used to find the total mass of cloud (gas) within the molecular cloud.

3.3 Inclination Angle

The inclination angle of the dust cloud is the angle subtended by the line of sight to the normal to the plane of the dust cloud. It is calculated using the Holmberg (1946) [26] formula, which is given as:

$$\cos^2 i = \frac{(b/a)^2 - (q^*)^2}{1 - (q^*)^2} \quad (4)$$

where a and b are the major and minor axes of the cloud, and q^* is the intrinsic flatness, which describes the internal morphology. For a molecular cloud dominated by neutral particles, its value is taken as 0.23 [27]. The cloud is said to *edge-on* if $i > 45^o$ and *face-on* if $i < 45^o$ [28].

3.4 Jeans Criteria

The process of stellar evolution initiates in the molecular cloud if the cloud has enough mass to enrich the gravitational compression against the gas pressure. The Jeans criteria describe the minimum mass and size required to trigger the evolution process, which is a function of the density and temperature of the cloud. The density of a cloud having radius R is given as:

$$\rho = \left(\frac{3}{4\pi}\right)^{2/3} \frac{k_B T}{m_H G R^2} \quad (5)$$

where k_B, m_H, T, and G are the Boltzmann constant, mass of neutral hydrogen, dust color temperature, and universal gravitational constant, respectively. The Jeans mass is given as:

$$M_J = \left(\frac{k_B T}{m_H G}\right)^{3/2} \left(\frac{1}{\rho}\right)^{1/2} \quad (6)$$

To initiate the gravitational process the mass of the cloud must be greater than the Jeans mass of the cloud [29].

3.5 Gaussian Distribution

For any natural process, we always expect the Gaussian distribution if the size of the variables is large. For a continuous random variable x having mean μ and standard deviation σ, the Gaussian probability distribution function is given by:

$$f(x) = \frac{1}{\sigma\sqrt{2\pi}} \exp\left(-\frac{(x-\mu)^2}{2\sigma^2}\right) \quad (7)$$

4 Results and Discussion

4.1 Structure and Size

In far infrared image the part of the W51 molecular cloud under study has prominent emission in both IRIS and AKARI map. In IRIS map it is single and isolated and elongated along North-South direction. But in AKARI map the core part is broken into two parts. In this paper these two parts are represented by AKARI-I and AKARI-II. The detail information about the center of the each structure, total size and size of isolated region is presented in Table 1. The pixels corresponds to maximum infrared flux in long wavelength infrared data, 100 μm in IRIS and 140 μm in AKARI data, is considered as a center of the structure under study. In all three structures, the center of the structure is slightly beyond the geometrical center. The physical center is the point corresponding to the pixels having maximum flux. In this work, the size of the pixels used on the FITS image are 1.5 arcmin/pixels in IRIS map and 0.25 arcmin/pixels in AKARI map. Fig. 2 shows the FITS view in Aladin v2.5 [30] at longer wavelength (100 μm in IRIS and 140 μm in AKARI) in all three sub-structures. The major and minor axis of the isolated region of each structure can also be seen in Fig. 2. The different contours seen in the FITS image are the isoflux contour lines.

Table 1: The table presents the geometrical center, center of structure with maximum flux, and size of both total square region and isolated region.

Structure	**Geometrical Center (RA, DEC [ICRS])**	**Center of Structure (RA, DEC [ICRS])**	**Size of Structure**		**Inclination Angle (i)**
			Total	**Isolated**	
IRIS-UP	290.910° +14.510°	290.935° +14.513°	0.45° × 0.45°	0.32° × 0.18°	59.19°
AKARI-I	290.920° +14.520°	290.934° +14.506°	0.15° × 0.15°	0.14° × 0.07°	62.89°
AKARI-II	290.798° +14.456°	290.797° +14.447°	0.10° × 0.10°	0.09° × 0.06°	50.01°

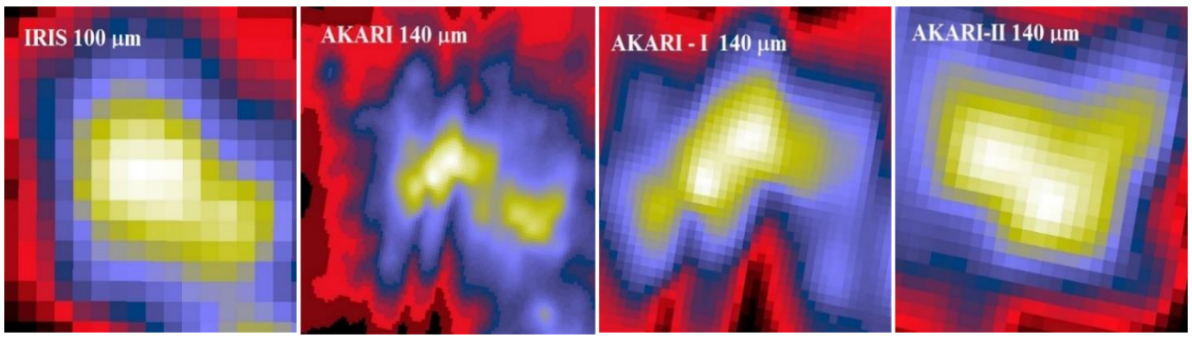

Figure 1: The JPEG image of the dust cloud nearby the W51 Molecular Cloud is shown in figure. The figure are for IRIS 100 μm, AKARI 140 μm, AKARI-I 140 μm, and AKARI-II 140 μm, from left to right respectively. In AKARI 140 μm (second) figure dust cloud is seen broken clearly into two parts; AKARI-I and AKARI-II.

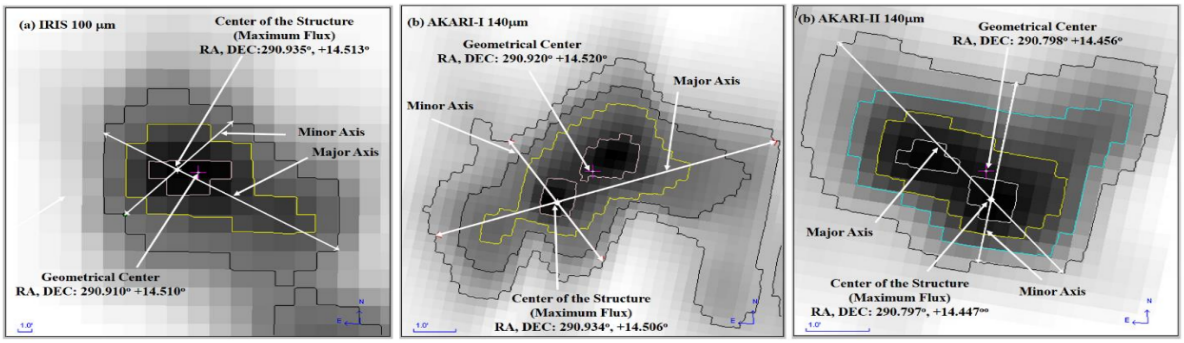

Figure 2: Aladin v2.5 view of the FITS image in IRIS (100 μm) and AKARI (140 μm) can be seen. In AKARI there are two structures; AKARI-I and AKARI-II. The geometrical center, maximum flux region (center of structure), major and minor axis are shown. The different contour line are isocontours with different values for three image. The region inside the outer isocontour is descried as an isolated region and is considered separately for analysis of the result in following section.

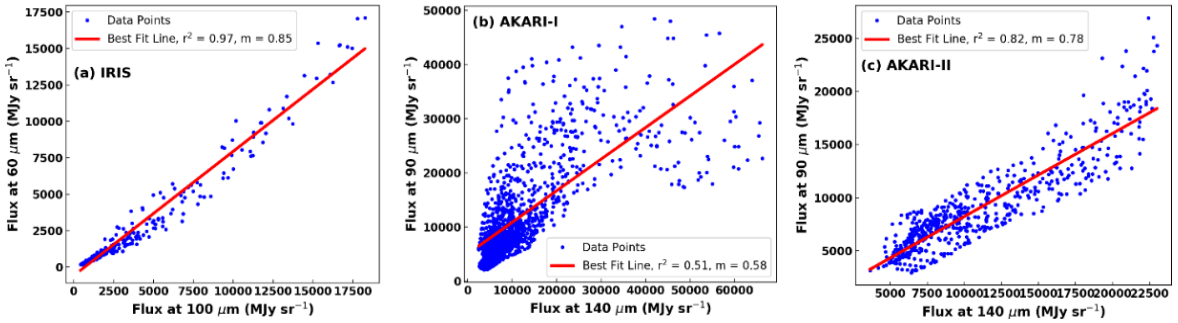

Figure 3: The figure shows the linear relation between two infrared fluxes in IRIS (a) and AKARI (b and c) data for total region. Here, r^2 is the coefficient of determination and m is slope of straight line.

Table 2: Statistical information of infrared flux; maximum (F_{max}), minimum (F_{min}), average (F_{av}), range, standard deviation (σ_F), and standard error (SE) at both wavelengths in dust structures in IRIS and AKARI data.

Structure	λ (μm)	**Infrared Flux (MJy sr^{-1})**				
		$\mathbf{F}_{max}$	$\mathbf{F}_{min}$	$\mathbf{F}_{av} \pm$ **S.E.**	$\mathbf{F}_{range}$	σ_F
IRIS	60	17090.00	158.15	2346.46 ± 184.65	16932.37	3323.61
	100	18277.80	427.97	3442.17 ± 212.98	17849.83	3833.71
AKARI-I	90	48455.82	2128.55	12161.23 ± 246.98	46327.28	8891.23
	140	66261.41	2452.37	12230.88 ± 302.41	63809.04	10886.73
AKARI-II	90	26890.39	2959.25	8947.48 ± 175.98	23931.14	4223.62
	140	23011.31	3643.55	10923.17 ± 204.30	19367.76	4903.08

4.2 Infrared Flux Density

The FITS image is processed in Aladin v10.0 [30] software to extract the infrared flux density at two wavelengths, 60 μm and 100 μm in IRIS data and 90 μm and 140 μm in AKARI data. The W51 molecular cloud and its both parts under study lie close to the galactic plane of the Milky Way Galaxy; therefore, the infrared flux density is very high at all wavelengths under study.

The information about the maximum, minimum, average, range, and standard deviation of the infrared flux in each wavelength for all structures can be seen in Table 2. Infrared flux is higher for AKARI data compared to IRIS data at both wave-

Table 3: The table presents the maximum (T_{max}), minimum (T_{min}), average (T_{av}), range, and standard deviation (SD) of T_d in total and isolated regions within the W51 molecular cloud.

Structure	Region	T_{max} (K)	T_{min} (K)	Tav ± S.E. (K)	T_{range} (K)	σ_T (K)
IRIS	Total	38.55 ± 4.10	25.29 ± 2.52	30.34 ± 0.16	13.26 ± 3.13	2.82
	Isolated	37.63 ± 2.09	28.49 ± 2.48	33.45 ± 0.27	9.14 ± 2.28	2.35
AKARI-I	Total	77.12 ± 24.86	17.01 ± 5.20	27.40 ± 0.21	60.11 ± 15.03	7.73
	Isolated	59.56 ± 17.20	17.01 ± 4.08	25.17 ± 0.23	42.55 ± 10.64	5.40
AKARI-II	Total	30.82 ± 3.64	18.85 ± 2.30	23.55 ± 0.08	11.87 ± 2.98	1.99
	Isolated	27.81 ± 2.38	20.26 ± 1.40	23.06 ± 0.10	7.55 ± 1.89	1.59

Table 4: The table shows the parameters in the linear fit, where r^2 is the coefficient of determination and T is the dust color temperature calculated using the slope.

Structure	Region	Best fit equation	r^2	T(K)	ΔT (K)
IRIS	Total	$F_S = 0.85F_L - 588.35$	0.97	35.37	−5.03
	Isolated	$F_S = 0.98F_L - 1946.38$	0.94	37.30	−3.85
AKARI-I	Total	$F_S = 0.58F_L + 5029.49$	0.50	20.57	+6.83
	Isolated	$F_S = 0.47F_L - 8504.23$	0.37	19.09	+6.08
AKARI-II	Total	$F_S = 0.78F_L + 415.54$	0.82	23.00	−0.55
	Isolated	$F_S = 0.93F_L - 2131.05$	0.70	24.71	+1.65

lengths. The flux is greater at long wavelengths for IRIS and AKARI-I structure, whereas for AKARI-II, the maximum value of flux at short wavelength is higher, but the average value is again lower at short wavelengths.

Furthermore, a linear relationship is found between the flux at two wavelength both in IRIS and AKARI data. The infrared flux of total square region as well as that of isolated region of all three structures is studied using the linear regression. For this study the infrared flux at long wavelength (F_L) is taken along the X-axis and short wavelength (F_S) is taken along the Y-axis, shown in Fig 3. The coefficient of determination (r^2) tells how closely the fitted data (red line) agree with the original data set (blue dots). It is found r^2 is more for total square region compare to isolated region. In IRIS data it is very well fitted but in AKARI-I it is just acceptable for total data and bad fit for isolated data. For AKARI-II, it is good fit. The various information related to the regression study is presented in Table 4 and the graph showing the linear relationship between two infrared fluxes is seen in Fig. 4. For AKARI-I, we found large number of background sources, such as; stars, clusters, YSO, different radio sources, HII region, infrared sources, etc., which can be seen in Fig. 10 (d e). Also, the Gaussian distribution of temperature is found more deviated from normal bell shape in Fig. 7(b). Moreover, the color map of infrared flux also shows the different nature of map for two wavelength in Fig. 5 (a b). These all studies tell us the poor relation between infrared flux at two wavelength for AKARI-I region.

4.3 Dust Color Temperature

We use the method given by Wood et al. (1994) [22] and Schnee et al. (2005) [23] to estimate the dust color temperature (T_d) of the interstellar dust cloud, dependent on infrared flux density at two wavelengths for which the spectral emissivity index (β) is taken as 2, assuming the interstellar dust having crystalline dielectric characteristic [31]. Table 3 presents various statistical information related to T_d for both the total square region as well as the isolated region in all three structures. The error in the average temperature (T_{av}) is the standard error ($\sigma_T/\sqrt{n}$), σ_T is the standard deviation, and n is the size of the data). But for maximum are minimum temperature are the half of the deviation from average value is taken. For range the average error in maximum and minimum value is used. The T_d is found more for AKARI data compare to the IRIS. However, the minimum value is less in AKARI. The range is found more than 5 K in both IRIS and AKARI data representing the dust cloud is thermally dynamic. Moreover, T_d and its range in AKARI-II is found more than AKARI-I, representing high thermal activities in AKARI-I. The T_d is found more in IRIS data compare to AKARI data. This is according to Wien's displacement law, which says the temperature is inversely proportional to wavelength. Furthermore, it is seen that the higher value of maximum T_d is found in AKARI-I. In AKARI-I, the contour map (Fig. 5(c)) as well as the Gaussian plot of temperature (Fig.7) shows the high temperature (more than 50 K) is found only in small regions or pixels. Most of the region have temperature less than 40 K. In IRIS and AKARI-I the distribution of the temperature

Table 5: Dust and gas mass (kg and solar mass ($M_\odot$) in dust structures and sub-structures.

Structure	**Region**	**M_d**		Mean per Pixels (kg)	**Gas Mass (kg)**	
		(in kg)	**(in $M_\odot$)**		(in kg)	**(in $M_\odot$)**
IRIS	Total	3.09×10^{32}	155.38	9.54×10^{29}	4.64×10^{34}	23307.50
	Isolated	1.51×10^{32}	76.04	1.96×10^{30}	2.27×10^{34}	11406.70
AKARI-I	Total	1.23×10^{34}	6172.64	9.47×10^{30}	1.84×10^{36}	925896.56
	Isolated	9.96×10^{33}	5006.92	1.79×10^{31}	1.49×10^{36}	751038.71
AKARI-II	Total	4.47×10^{33}	2248.04	7.76×10^{30}	6.71×10^{35}	337205.43
	Isolated	2.73×10^{33}	1370.55	1.17×10^{31}	4.09×10^{35}	205582.88

is almost Gaussian. Also, the standard deviation is found maximum for the AKARI-I, suggesting the wide variation in the temperature distribution. The Gaussian distribution of the dust color temperature on total square region in all three structures is seen in Fig.7.

Additionally, the slope of the best fit straight line could give the average temperature. The slope (m) of the straight line is the ratio (R) of the infrared flux at two wavelengths, $R = \frac{F(\lambda_{\rm long})}{F(\lambda_{\rm short})}$. This provides some insight to calculate the temperature using equation (2). Using this method, temperature is calculated for both the total square region as well as in the isolated region. The results are presented in Table 4. The deviation in temperature (ΔT) between Table 3 and Table 4 is also presented. The deviation is due to the value of y-intercept (c). In the linear regression method we implement, $F_s = R \cdot F_{\rm L} + c$, rather than $F_s = R \cdot F_{\rm L}$. It is evident that the deviation is more for AKARI-I for which the data deviated much from Gaussian nature compare to other. For isolated region the deviation is less in IRIS and AKARI-I but for AKARI-II it is more. The background sources at the isolated region is very much crowded for IRIS and AKAARI-I compare to AKARI-II, which can be seen in Fig. 10.

4.4 Dust Mass

The mass of dust in each pixel of the dust structure is calculated using the infrared flux at long wavelength, dust color temperature, Planck's function, and the distance to the dust cloud using the method of Hildebrand (1984) [24] and Young et al., (1993) [25]. Planck's function is a function of temperature and wavelength. The distance to the W51 molecular cloud is taken as ∼17000 light years or ∼5410 pc [20].

The dust mass as well as the mass of gas within the total square region and isolated region of all three structures is presented in Table 5. The mass of dust within the isolated region is also calculated separately. Obviously, it is seen that the total dust mass in the isolated region is less than the total square region. One of the reasons is that the number of pixels included within the isolated region is less compared to the total square region. Another effective reason is that the average dust mass per pixel is slightly more in the isolated region compared to the total square region.

The mass of gas (M_g) is calculated using the fact that $M_g \approx 150 M_d$ [24]. Therefore, the mass of gas also follows the same trend as that of the dust mass within both the total square and isolated regions.

4.5 Contour Map

The visualization of the infrared flux at two wavelengths, dust color temperature, and dust mass is presented in Fig. 4, Fig. 5, and Fig. 6, respectively, for IRIS, AKARI-I, and AKARI-II. The contour maps of the infrared flux at 60 μm and 100 μm for the IRIS structure are almost identical, as described in the regression analysis with an r^2 value of 0.97. Infrared flux is decreasing almost smoothly from the center to the outer region in IRIS data. In AKARI-I, the contour maps are less identical; a clear donut shape with local minima at the geometrical central part is observed in infrared flux at 90 μm, and an unbalanced dumbbell shape elongated along the diagonal is observed in infrared flux at 140 μm. The regression analysis between the fluxes at two wavelengths also shows a moderate value of r^2, which is 0.50. For AKARI-II, the contour maps show quite a similar distribution, both elongated along the main diagonal of the square region with a slight rise towards the right-upper part. However, the maximum value of the flux is seen at 140 μm, which is different from AKARI-I. The regression analysis shows a quite good value of r^2, which is 0.82. The qualitative distribution inferred from the contour map is in accordance with the quantitative analysis provided by the regression method.

The IRIS data contour map of the dust color temperature (T_d) also appears elongated along the main diagonal of the square region, but the overall distribution is quite different compared to the flux at both wavelengths. The maximum value of the temperature is beyond the center with maximum flux. Also, the temperature is not decreasing smoothly from the maximum value towards the outer regions; however, an isolated region is

observed elongated along the main diagonal. In AKARI-I, the color map of the dust color temperature is very different from the infrared flux. An isolated low-temperature cavity can be seen within the region of interest, which is quite interesting. The maximum temperature is also deviated from the center, and the variation is also not smooth from its maximum value towards the outer region. Only very few pixels have a higher temperature ($> 50K$), which can also be seen in the Gaussian distribution in Fig. 7. In AKARI-II, the color map shows variation of T_d unevenly breaking into multiple subregions with multiple local minimum. The maximum temperature lies at the lower-mid-edge of the square region. The contour map of the dust mass in IRIS structure seems like the color map of flux at both wavelength. It shows the two maxima region at core. The pixels having maximum mass lies very close to the pixels having maximum flux. In outer region, the dust mass decreases smoothly showing the symmetric variation. A visual comparison between contour map of dust color temperature and dust mass shows a very poor correlation. In AKARI-I structure, the contour map of dust mass shows double maxima, concentrated near the center and elongated along the off-diagonal of square region. The mass distribution is quite similar to the infrared flux at core region at 140 μm. The contour map of temperature and mass are seen nearly inverse within the core region. The background sources, such as; HII region, infrared, mid-infrared, near infrared, etc., are crowed near the isolated cavity of temperature which might be contributing huge dust at core. In AKARI-II, the contour map of the dust color temperature is entirely different from the infrared flux at both wavelength. It is breaking unevenly into three sub-clumps. The background sources shown in Fig 10 (c) also shows crowd of background sources in the periphery of the region where the aggregation of the dust mass is more. This is an evident that the dust mass is pushed slightly far away from the background sources. The visual comparison shows the distribution of mass almost inverse of the temperature. The quantitative relationship between temperature and mass is presented in later section.

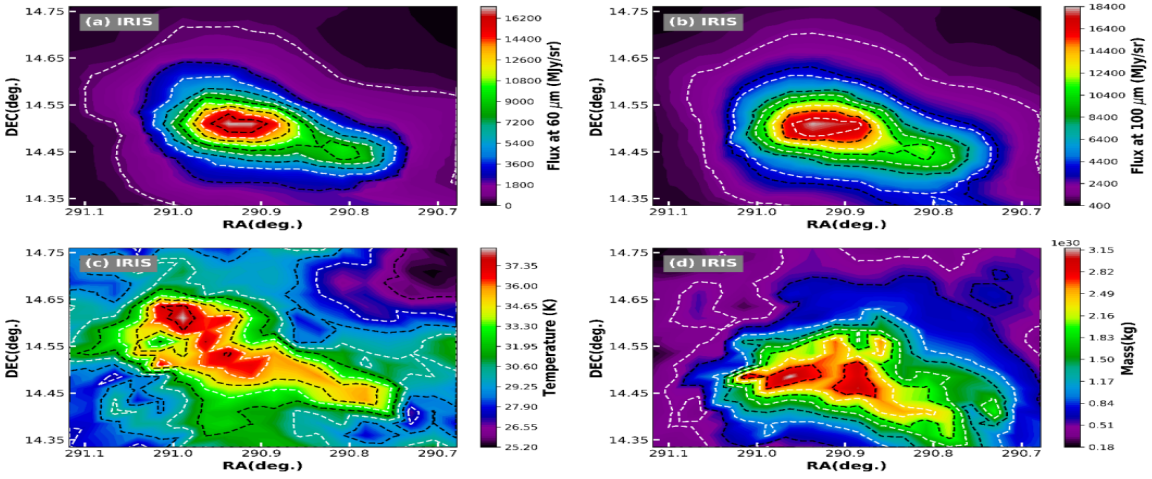

Figure 4: The contour map for infrared fluxes (a and b), dust color temperature (c) and dust mass (d) for whole dust structure around W51 Molecular Cloud in IRIS map overlaid with the contour at different levels, in the interval of $(\bar{X} \pm k.\sigma)$, $\bar{X}$ and σ are the mean and standard deviation of corresponding quantities, and k is the constant chosen in such a way that the contours are distributed evenly. The value of constant k is chosen [-0.5, 0, 0.5, 1, 1.5, 2.0, 2.5, 3, 3.5, 4] for flux at 60 μm, [-0.5, 0, 0.2, 1.0, 1.5, 2.0, 2.5, 3.0, 3.5] for flux at 100 μm, [-2.0, -1.5, -1.0, -0.5, 0, 0.5, 1, 1.5, 2.0, 2.5] for T_d and [-0.75, -0.5, 0, 0.5, 1.0, 1.5, 2.0, 2.5] for M_d for outer to inner contour.

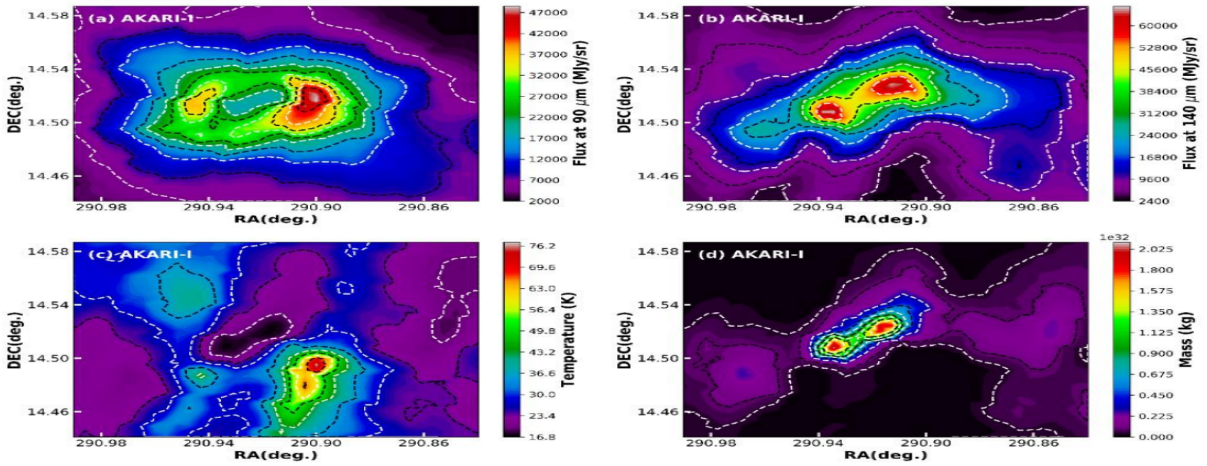

Figure 5: The contour map for infrared fluxes (a and b), dust color temperature (c) and dust mass (d) for upper dust structure (AKARI-I) around W51 Molecular Cloud in AKARI-I map overlaid with the contour at different levels, in the interval of $(\bar{X} \pm k.\sigma), \bar{X}$ and σ are the mean and standard deviation of corresponding quantities, and k is the constant chosen in such a way that the contours are distributed evenly. The value of k is chosen [-0.75, -0.45, 0, 0.5, 1.0, 1.5, 2.0, 2.5, 3.0, 3.5] for flux at 90 μm, [-0.75, -0.5, -0.20, 0, 0.5, 1.0, 2.0, 3.0, 4.0] for flux at 140 μm, [-1.0, -0.5, 0, 1.0, 2.0, 3.0, 4.0, 5.0] for T_d and [-0.25, 0, 1.0, 2.0, 3.0, 4.0, 5.0, 6.0, 7.0] for M_d form outer to inner contour.

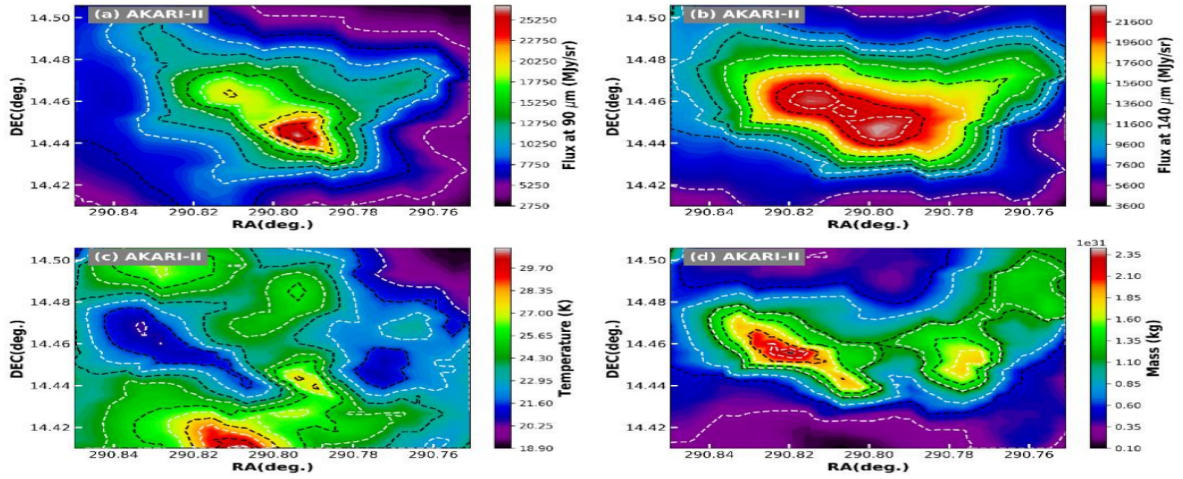

Figure 6: The contour map for infrared fluxes (a and b), dust color temperature (T_d) (c) and dust mass (M_d) (d) for lower dust structure (AKARI-II) around W51 Molecular Cloud in AKARI map overlaid with the contour at different levels, in the interval of $(\bar{X} \pm k.\sigma), \bar{X}$ and σ are the mean and standard deviation of corresponding quantities, and k is the constant chosen in such a way that the contours are distributed evenly. And the value of k are [1.0, -0.5, 0, 0.5, 1.0, 1.5, 2.0, 2.5, 3.0, 3.5] for flux at 90 μm, [-1.0, -0.5,-0.25, 0, 0.5, 1.0, 1.5, 2.0, 2.25] for flux at 140 μm, [-1.5, -1.0, 0.5, 0, 0.5, 1.0, 1.5, 2.0, 2.5, 3.0, 3.5] for T_d and [-1.0, -0.5, 0, 0.9, 1.0, 1.5, 2.0, 2.5, 3.5] for M_d form outer to inner contour.

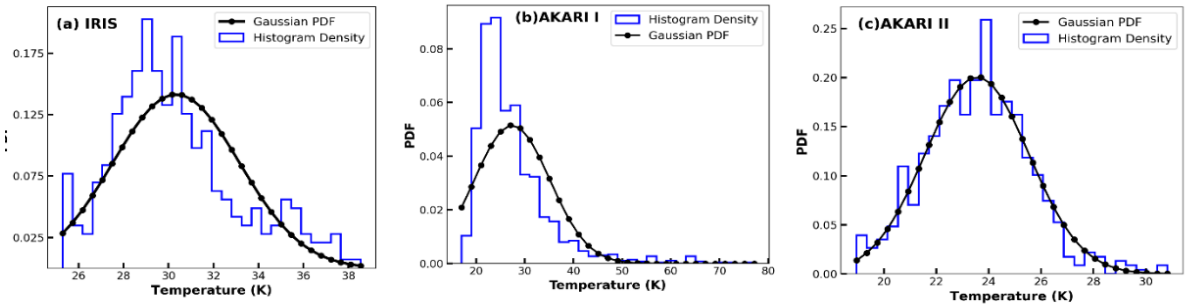

Figure 7: Figure shows the Gaussian distribution for dust color temperature for all structures. In all figure the quantities dust color temperature is taken along X-axis and their Gaussian PDF are taken along Y-axis.

4.6 Flux-Temperature-Mass Relation

The color map with contour is quite effective to understand the spatial distribution of the infrared flux, dust color temperature and dust mass. For a quantitative analysis the color map is not adequate to give the proper information. The linear regression is used to quantify the relationship between them. The coefficient of determination (r^2) is calculated for each pair of variables in all dust structure. The selected plots for which the $r^2 > 0.50$ are presented in Fig. 8. The temperature (T_d) is found to be increased with flux at both wavelength in IRIS data but no clear relation for AKARI data. Also, the dust mass (M_d) is found to be increase with increase in infrared flux at both wavelength, both IRIS and AKARI data. But for flux at short wavelength the r^2 >0.50 for both region in AKARI. In overall, it can be said that the T_d and M_d both increases with increase in infrared flux in all regions. The graph between Td and M_d is shown Fig. 9, in which all the plots have poor coefficient of determination, $r^2 > 0.50$. However, in IRIS and AKARI data a very clear difference can be seen. In IRIS data, the relation is direct where as in AKARI, in both graph, the relation is inverse. Moreover, the data in IRIS is more scattered compare to AKARI data. The value of r^2 for each pair of variables is presented in Table 6.

4.7 SIMBAD Background Source

Study of the background objects within the selected region is carried out with the help of catalog available in SIMBAD. The Fig. 10 shows the background sources overlaid in the isocontour lines that are same for infrared flux at longer wavelength, i.e., 100 μm for IRIS and 140 µm for AKARI–I and AKARI-II. In this work, the Young stellar object (YSO), YSO candidates, different varieties of the radio sources, dark nebula, interstellar bubbles, HII region, star, dense core, part of cloud, etc., are numerous. For the better visualization the background objects are presented in three graph in IRIS data and two graph in AKARI-I data and single graph in AKARI-II. The number of background sources within the region of IRIS structure is 1364, within AKARI-I structure is 401 and within AKARI-II structure 134. There are least but very important objects, like HII region, Infrared (IR), Mid IR, Far IR, dense core bubble, star forming regions, radio sources, etc., which are found to be concentrated within the core region of the cloud and it can be concluded that they are responsible for the huge infrared flux, temperature and mass as seen in color map of IRIS in Fig. 4. The background objects around AKARI-I is more compare to AKARI-II, the effect of which can be seen in the average value, range and Gaussian curve of T_d. The range of T_d is more than 40 K for isolated region and more than 60 K for total square region which is very high compare to AKARI-II [Table 3], which represents more thermal instability in AKARI-II due to the presentence of background sources. Also, Gaussian distribution of T_d is much deviated from Normal bell shape. The color map also shows the effect of background objects in both of the AKARI structures. Cavity of cold and massive dust region is seen in the periphery of regions where background sources are crowded. Therefore, the entire dust properties, such as infrared flux, dust color temperature and dust mass can be explained on the basis of the background objects.

4.8 Density and Jeans Mass

The isolated region in each dust structure as seen in Fig. 2 is studied separately for the Jeans criteria, whether the mass of the cloud under the isolated structure is sufficient or not to trigger the star formation process is checked. The average size, average temperature, density, Jeans mass and total mass of cloud of isolated region within clouds in IRIS, AKARI-I and AKARI-II are presented in Table 7. From Table 1 it is clear that the size of the IRIS structure is largest and AKARI-II is smallest.

Conversely, the density of the AKARI-II is found maximum and IRIS is minimum. But, the Jeans mass (M_J) is maximum for IRIS structure due to its large size. The value of M_J is found less than the mass of the cloud in all structures. It is seen that there is no any possibility of further collapse of clouds either singly or part wise for the star formation process in the future.

Table 6: The coefficient of determination (r^2) for each pair of variables, F_S and F_L represents the flux at short and long wavelength.

	coefficient of determination (r^2)				
	F_L vs T_d	F_S vs T_d	F_L vs M_d	F_S vs M_d	T_d vs M_d
IRIS	0.56	0.54	0.65	0.81	0.21
AKARI-I	0.24	0.05	0.07	0.79	0.23
AKARI-II	0.05	0.02	0.19	0.59	0.47

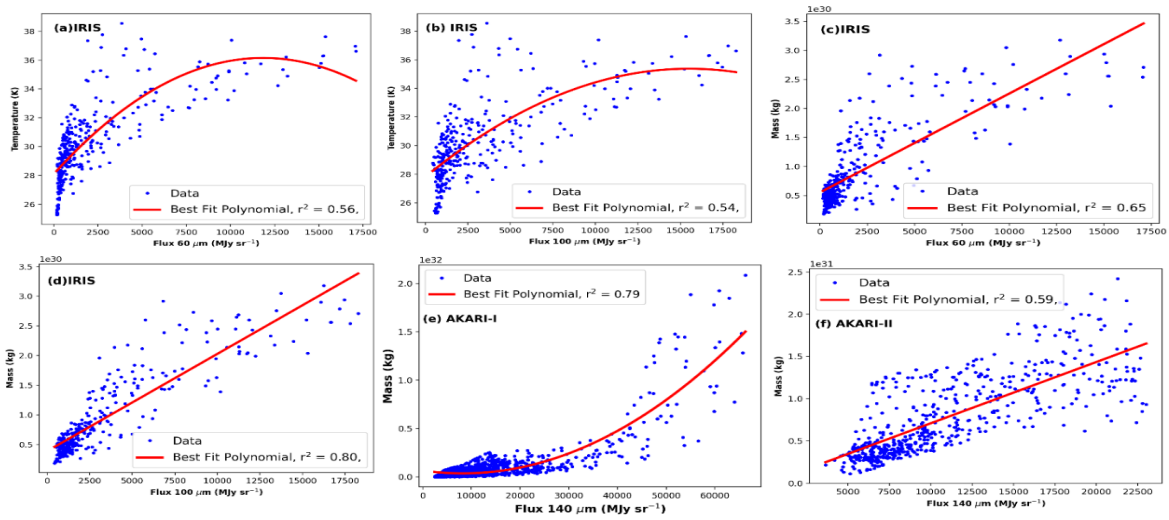

Figure 8: The best fit straight line between the infrared flux, dust color temperature and dust mass in IRIS data. The r^2 represents the correlation coefficient. The plot with $r^2 < 0.50$ are not included here.

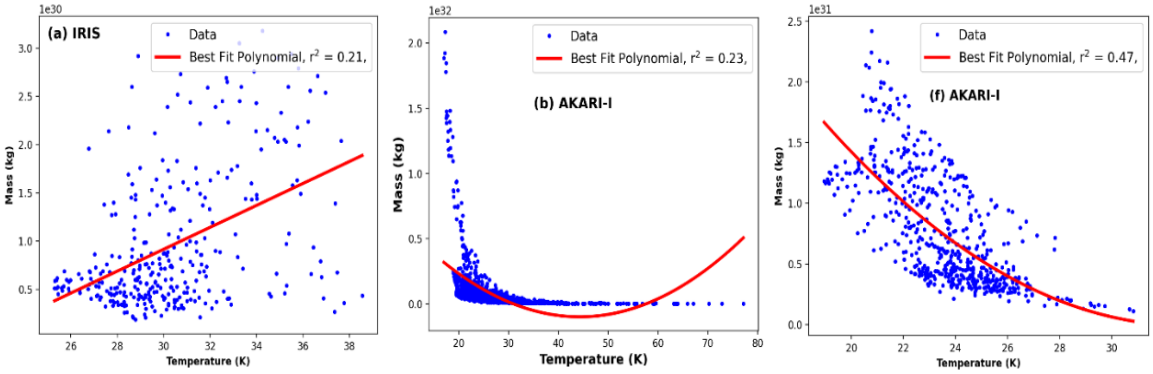

Figure 9: The best fit line between the T_d and M_d is seen in IRIS (a), AKARI-I (b) and AKARI-II (c) is shown. In all data a poor correlation is observed.

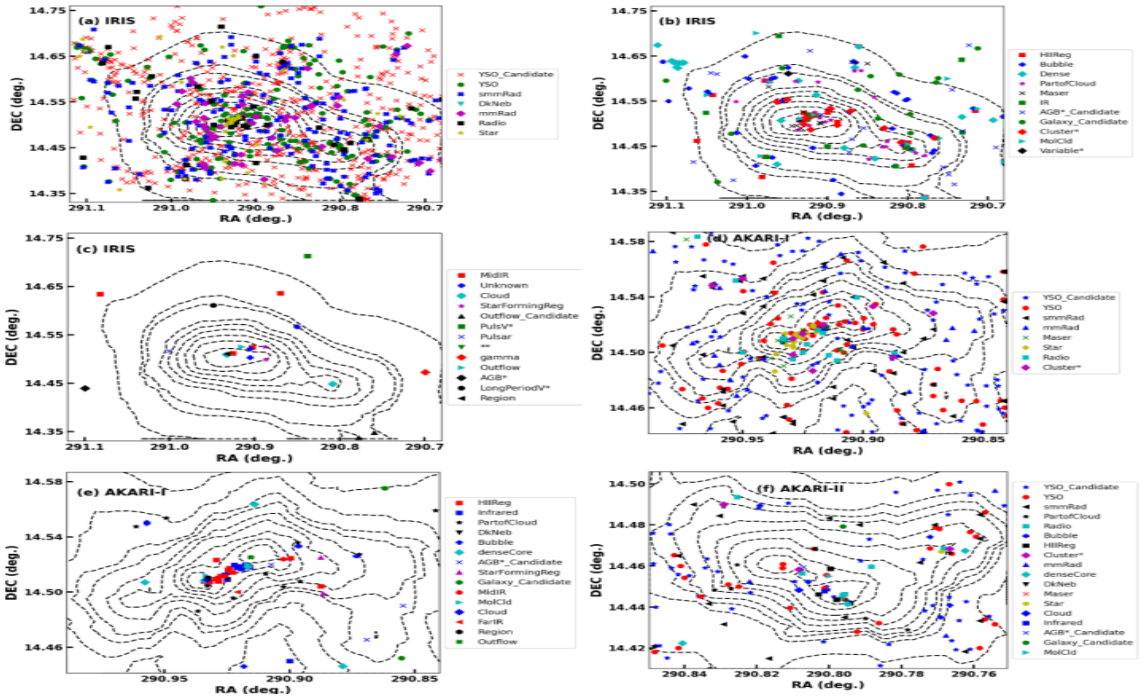

Figure 10: The figure shows the SIMBAD sources around W51 molecular cloud, for IRIS (a, b and c), AKARI-I (d and e) and AKARI-II (f). In all plot, RA is taken along X-axis, DEC is taken along Y-axis. The name of sources in the legend is according to the SIMBAD. For IRIS and AKARI-I there are more graph made for the better visualization of the numerous objects.

Table 7: Average radius, dust color temperature, density, Jeans mass, and total mass of cloud in isolated regions of IRIS, AKARI-I, and AKARI-II.

Structure	**Radius (m)**	**T_d (K)**	**Density (kg/m^3)**	**Jeans Mass**		**Cloud Mass**	
				(kg)	$M_\odot$	(kg)	$M_\odot$
IRIS	6.07×10^{15}	33.45	4.33×10^{-17}	4.05×10^{31}	20.36	2.27×10^{34}	11406.70
AKARI-I	2.55×10^{15}	25.17	1.85×10^{-16}	1.28×10^{31}	6.44	1.49×10^{36}	751038.71
AKARI-II	1.82×10^{15}	23.06	3.36×10^{-16}	8.39×10^{30}	4.22	4.09×10^{35}	205582.88

5 Conclusion

A comparative study of the properties of dust is performed within the molecular cloud W51 located at (RA, DEC) (ICRS): $290.910°, +14.510°$, having an angular size of $0.45° \times 0.45°$, using the IRIS and AKARI data. Following are the major conclusions:

1. Being situated in the galactic plane, the dust cloud is very bright in both AKARI and IRIS. Furthermore, it is divided into two isolated sub-structures having angular sizes of $0.15° \times 0.15°$ and $0.10° \times 0.10°$ in the AKARI map, represented as AKARI-I and AKARI-II, respectively.

2. The average dust color temperature is found to decrease in the isolated region compared to the total region in all sub-structures. The hot region is found to lie outside the isolated region.

3. The dust color temperature follows Wien's displacement law, meaning the temperature is inversely proportional to wavelength. A lower temperature is found for AKARI data compared to IRIS data.

4. The range of temperature in all structures is found to be more than 10 K in total and 5 K in the isolated region, indicating that the structure is far from thermal stability. In AKARI-I, the range is very high, representing huge thermal instability compared to AKARI-II.

5. The regression analysis shows a linear relationship between the infrared flux at two wavelengths in IRIS and AKARI-II, but the relation is very poor in AKARI-I for the isolated region. This might be the consequence of the large range in temperature. A mixed type (linear and quadratic) of relationship is

found between the infrared flux, dust color temperature, and dust mass.

6. The regression analysis shows that T_d is poorly correlated with M_d. In IRIS data, M_d is directly proportional to T_d, but for AKARI, M_d is inverse to T_d.

7. The dust mass is found to be more in both AKARI maps compared to IRIS map, even though the dust structure in IRIS is larger in size. Moreover, the mass per pixel is more for AKARI maps. The mass per pixel is more in the isolated region for both IRIS and AKARI maps.

8. The SIMBAD point sources within the study region show a large number of stars, young stellar objects (YSO), interstellar medium (ISM) sources, etc. YSOs, stars, radio sources, masers, HII regions, infrared sources, mid-infrared sources, etc., are mostly found within the core region of AKARI-I and AKARI-II structures. This is the manifestation of the huge infrared flux within the core region.

9. The study of density and Jeans criteria shows that the dust structure is denser in AKARI data compared to IRIS data. Also, AKARI-II is found to be denser than AKARI-I. Furthermore, all dust clouds deny the possibility of star formation.

Acknowledgements

The authors want to acknowledgment to their host institution Department of Physics, Tri-Chandra Multiple Campus and Central Department of Physics, TU for all types of academic support in this research work. Thanks to SkyView Virtual Observatory and SIMBAD for the data used in this work.

References

[1] I. A. Bonnell and M. R. Bate. Star formation through gravitational collapse and competitive accretion. *Monthly Notices of the Royal Astronomical Society*, 370(1):488–494, 2006.

[2] G. Westerhout. A survey of the continuous radiation from the galactic system at a frequency of 1390 mc/s. *Bulletin of the Astronomical Institutes of the Netherlands*, 14:215, 1958.

[3] J. M. Carpenter and D. B. Sanders. The w51 giant molecular cloud. *The Astronomical Journal*, 116(4):1856, 1998.

[4] M. S. Nanda Kumar, U. S. Kamath, and C. J. Davis. Embedded star clusters in the w51 giant. *Monthly Notices of the Royal Astronomical Society*, 353:1025–1034, 2004.

[5] M. Kang, J. H. Bieging, M. S. Povich, and Y. Lee. Embedded young stellar object candidates in the active star-forming complex w51: Mass function and spatial distribution. *The Astrophysical Journal*, 706(1):83, 2009.

[6] G. Neugebauer, H. Habing, R. Van Duinen, H. Aumann, B. Baud, and et al. The infrared astronomical satellite (iras) mission. *The Astrophysical Journal*, 278:L1–L6, 1984.

[7] A. S. Ferrarotti and H. P. Gail. Mineral formation in stellar winds-ii. effects of mg/si abundance variations on dust composition in agb stars. *Astronomy & Astrophysics*, 371(1):133–151, 2001.

[8] M. J. Barlow. The destruction and growth of dust grains in interstellar space–i. destruction by sputtering. *Monthly Notices of the Royal Astronomical Society*, 183:367–395, 1978.

[9] M. A. Miville-Deschênes and G. Lagache. Iris: a new generation of iras maps. *The Astrophysical Journal Supplement Series*, 157:302, 1995.

[10] H. Murakami, H. Baba, P. Barthel, D. L. Clements, M. Cohen, and et al. The infrared astronomical mission akari. *Publications of the Astronomical Society of Japan*, 59:S369–S376, 2007.

[11] E. L. Wright, P. R. Eisenhardt, A. K. Mainzer, M. E. Ressler, R. M. Cutri, and et al. The wide-field infrared survey explorer (wise): mission description and initial on-orbit performance. *The Astronomical Journal*, 140:1868, 2010.

[12] S. Bhattarai, M. S. Paudel, S. N. Yadav, and A. K. Jha. Properties of dust in the northeast part of perseus cloud within the open cluster ic 348 using data from iris and akari. *BIBECHANA*, 20(1):92–102, 2023.

[13] M. S. Paudel. Studies of dust properties in substructures around white dwarf wd 0307+077 in iris survey. *Journal of Nepal Physical Society*, 8:39–47, 2022.

[14] S. Sigdel, S. Rijal, and M. S. Paudel. Comparative study of dust properties around white dwarf pg 1227-079 in iris and akari survey. *Journal of Nepal Physical Society*, 8(3):79–92, 2022.

[15] S. Rijal, S. Sigdel, and M. S. Paudel. Study of an isolated dust structure nearby the white dwarf wd0011-399 using iris, akari and wise data. *Journal of Nepal Physical Society*, 8(2):14–22, 2022.

[16] M. S. Paudel. Studies of the properties of dust structure nearby the supernova remnants g053. 41+ 00.3, g053. 9+ 00.2 and g053. 1+ 00.3 using data from iris and akari. *Journal of Nepal Physical Society*, 7(3):59–66, 2021.

[17] M. S. Paudel, P. Bhandari, and S. Bhattarai. Study of dust cavity around the white dwarf wd 0352-049 in infrared astronomical satellite map. *Journal of Nepal Physical Society*, 7(2):110–118, 2021.

[18] R. Kandel, A. Chaudhary, K. Chaudhary, M. Jalan, A. Subedi, K. Khatiwada, and A. K. Jha. Distribution of dust color temperature, dust mass and planck's function around c-rich agb star: Iras 19558+ 3333 using iris, akari, and wise surveys. *Scientific World*, 16(16):21–27, 2023.

[19] A. Thapa, M. S. Paudel, and B. Pant. An infrared survey of isolated nebular structures at galactic latitudes 16.98° & 1.98° in iras map. *Journal of Nepal Physical Society*, 5:74–84, 2019.

[20] R. Genzel, D. Downes, M. H. Schneps, M. J. Reid, J. M. Moran, L. R. Kogan, and B. Ronnang. Proper motions and distances of h2o maser sources. ii-w51 main. *The Astrophysical Journal*, 247:1039–1051, 1981.

[21] M. Wenger, F. Ochsenbein, D. Egret, P. Dubois, F. Bonnarel, S. Borde, F. Genova, G. Jasniewicz, S. Lalo'e, S. Lesteven, and R. Monier. The simbad astronomical database-the cds reference database for astronomical objects. *Astronomy and Astrophysics Supplement Series*, 143(1):9–22, 2000.

[22] D. O. Wood, P. C. Myers, and D. A. Daugherty. Iras images of nearby dark clouds. *The Astrophysical Journal Supplement Series*, 95:457–501, 1994.

[23] S. L. Schnee, N. A. Ridge, A. A. Goodman, and J. G. Li. A complete look at the use of iras emission maps to estimate extinction and dust temperature. *The Astrophysical Journal*, 634:442, 2005.

[24] R. H. Hildebrand. The determination of cloud masses and dust characteristics from submillimeter thermal emission. *Quarterly Journal of the Royal Astronomical Society*, 24:267, 1983.

[25] K. Young, T. Phillips, and G. Knapp. Circumstellar shells resolved in iras survey data. ii-analysis. *The Astrophysical Journal*, 409:725–738, 1993.

[26] E. Holmberg. On the apparent diameters and the orientation in space of extragalactic nebulae. *Meddelanden fran Lunds Astronomiska Observatorium Serie II*, 117:3–82, 1946.

[27] M. P. Haynes and R. Giovanelli. Neutral hydrogen in isolated galaxies. iv-results for the arecibo sample. *The Astronomical Journal*, 89:758–800, 1984.

[28] A. Jha and B. Aryal. A study of a cavity nearby a pulsar at-60º latitude in the far infrared map. *Journal of Nepal Physical Society*, 4:33–41, 2017.

[29] C. Low and D. Lynden-Bell. The minimum jeans mass or when fragmentation must stop. *Monthly Notices of the Royal Astronomical Society*, 176(2):367–390, 1976.

[30] F. Bonnarel, P. Fernique, O. Bienaymé, D. Egret, F. Genova, and et al. The aladin interactive sky atlas-a reference tool for identification of astronomical sources. *Astronomy and Astrophysics Supplement Series*, 143:33–40, 2000.

[31] X. Dupac, J. P. Bernard, N. Boudet, M. Giard, J. M. Lamarre, and et al. Inverse temperature dependence of the dust submillimeter spectral index. *Astronomy & Astrophysics*, 404:L11–L15, 2003.